Nanoscale

PAPER

Cite this: *Nanoscale*, 2015, **7**, 1167

Origin of electrochemical activity in nano-Li_2MnO_3; stabilization *via* a 'point defect scaffold'

Thi X. T. Sayle,[a,b] Francesco Caddeo,[a] Nkwe O. Monama,[b,c] Kenneth M. Kgatwane,[b] Phuti E. Ngoepe[b] and Dean C. Sayle*[a]

Received 22nd September 2014,
Accepted 17th November 2014

DOI: 10.1039/c4nr05551a

www.rsc.org/nanoscale

Molecular dynamics (MD) simulations of the charging of Li_2MnO_3 reveal that the reason nanocrystalline-Li_2MnO_3 is electrochemically active, in contrast to the parent bulk-Li_2MnO_3, is because in the nanomaterial the tunnels, in which the Li ions reside, are held apart by Mn ions, which act as a pseudo 'point defect scaffold'. The Li ions are then able to diffuse, *via* a vacancy driven mechanism, throughout the nanomaterial in all spatial dimensions while the 'Mn defect scaffold' maintains the structural integrity of the layered structure during charging. Our findings reveal that oxides, which comprise cation disorder, can be potential candidates for electrodes in rechargeable Li-ion batteries. Moreover, we propose that the concept of a 'point defect scaffold' might manifest as a more general phenomenon, which can be exploited to engineer, for example, two or three-dimensional strain within a host material and can be fine-tuned to optimize properties, such as ionic conductivity.

Introduction

Rechargeable Li-ion batteries are able to capture, convert, store and release energy and are widely used to power devices spanning mobile phones to hybrid electric vehicles. Accordingly, considerable research efforts are directed in this technologically important area. Rechargeable Li-ion batteries normally operate (discharge) with Li deintercalating from a negative electrode (anode), passing through an electrolyte and intercalating into a positive electrode (cathode); charging is the reverse of this process.

Commercialization of Li ion batteries, for example in electric vehicles, requires high power output (fast charge/discharge rates). However, this is limited by the Li diffusivity within the solid and therefore depends upon the dimensions of the electrodes. Potentially, the intercalation/deintercalation processes using host electrodes with dimensions at the nanoscale, can be sufficiently quick to deliver the power required to make Li-ion driven electric vehicles viable.[1] Central to this research is the atomistic level understanding of Li mobility within the host electrodes. However, elucidating such mechanisms is difficult experimentally and therefore atomistic and quantum chemical computer simulations can be used to provide unique insight.[2,3]

Layered-layered oxide composite cathodes, typically of composition $xLi_2MnO_3{\cdot}(1-x)LiMO_2$, have attracted much attention, for essentially doubling the capacity available in the earlier generation of Li-ion batteries based on $LiCoO_2$.[4] However, their use is currently limited by, amongst others, voltage fade.[5] Hence, further studies on one of the end members of the composites, Li_2MnO_3, could shed valuable insights on such problems. Li_2MnO_3 is known to be electrochemically inactive in the parent bulk form and can be rendered Li-active by leaching Li or Li_2O from the structure; these Li-deficient compounds are reported to have high intercalation capacities and good reversibility.[6] Alternatively, when synthesized in a nanocrystalline form, Li_2MnO_3 has been shown to be electrochemically active, yielding capacities up to 200 mA h g^{-1}, and excellent capacity retention over multiple cycles.[7]

Here, we use MD simulation to generate atomistic models of nano-Li_2MnO_3 and interrogate the models to reveal the mechanism underpinning Li ion mobility and rationalise why the nanoform is electrochemically active whereas, conversely, the bulk form is inactive.

A typical simulation approach might be to construct an atomistic model of the perfect 'bulk' material (cathode) and calculate the energy barriers associated with Li mobility within the material. However, an atomistic model of the perfect bulk material is unlikely representative of the real nanomaterial, which will comprise a hierarchical structural complexity

[a]*School of Physical Sciences, University of Kent, Canterbury, CT2 7NZ, UK. E-mail: d.c.sayle@kent.ac.uk*
[b]*Materials Modelling Centre, University of Limpopo, Private Bag x1106, Sovenga, 0727, South Africa*
[c]*Centre for High Performance Computing, CSIR, 15 Lower Hope Rd, Cape Town 7700, South Africa*

including: polymorphic crystal structure, microstructural features such as grain-boundaries, dislocations and intrinsic point defects and nanostructure such as morphology and surfaces exposed. Such structural attributes are likely to influence profoundly the mobility of Li within the host material and must be captured within the model to enable reliable prediction. For example, the exposure of particular surfaces of the nanoparticle will result in relaxation of the surface ions. The impact upon Li mobility within these regions can potentially be profound because the size of the exit tunnel, through which the Li diffuses to deintercalate from the electrode, would change. Indeed, Tompsett and co-workers calculated, using Density Functional Theory (DFT), that the energy barrier to Li intercalation into β-MnO_2, *via* the (101) surface, is 0.6 eV, which is much higher than the 0.17 eV energy barrier calculated for mobility within the bulk material;[2] the β-MnO_2(101) surface dominates the morphology. However, this study used a model comprising a perfectly flat MnO_2(101) surface. Conversely, the surface of a nanomaterial can exhibit high curvature, which will depend upon the dimensions of the nanomaterial. Such curvatures will likely impact further upon the energy associated with intercalation/deintercalation processes. Similarly, the atomistic structure of the core region of a grain-boundary or dislocation will also differ markedly from the parent bulk material and will also likely influence the Li mobility.[8]

These studies illustrate that hierarchical structural features, such as surface morphology, dislocations, grain-boundaries play a pivotal role in the thermodynamics and kinetics of intercalation/deintercalation processes. Accordingly, to simulate the mobility of Li ions in nano-Li_2MnO_3 directly, requires all levels of hierarchical structural features to be captured within a *single* atomistic model. However, this is a challenging undertaking. For example, although nanoparticle morphologies can be cleaved from the parent bulk material[9] and symmetry operators used to introduce a dislocation or grain-boundary into the atomistic model, the structural configuration of dislocations and grain-boundaries in Li_2MnO_3 have not, thus far, been documented. Accordingly, the grain-boundary and dislocation configurations chosen may prove erroneous.

Structural complexity evolves within the real material during synthesis – specifically, during the 'crystallization step'. Accordingly, we simulated the crystallization process using molecular dynamics to capture the structural complexity within the models. The simulator is therefore not required to define (perhaps erroneously) the atomistic structure.

Method

In this section we outline the potential model used to describe nano-Li_2MnO_3; the computer code used to perform all the molecular dynamics (MD) simulations and the strategy used to generate an atomistic model for nano-Li_2MnO_3, which comprises a hierarchical structural complexity.

Potential model

All calculations, presented in this study, were based upon the Born model of the ionic solid, where the energy, E, of the system is given by:

$$E(r_{ij}) = \sum_{ij} \frac{Q_i Q_j}{4\pi\varepsilon_o r_{ij}} + \sum_{ij} A \exp\left(\frac{-r_{ij}}{\rho}\right) - C r_{ij}^{-6}$$

the first term represents the Coulombic interaction between ion i of charge Q_i and ion j of charge Q_j, which are a distance r_{ij} apart. The second term is of the Buckingham form, which is particularly effective in representing ionic solids. Model parameters are presented in Table 1 and were taken from ref. 10,11.

The structural parameters for Li_2MnO_3, derived using this potential model, are in accord with measured values, Table 1; we note that the potential parameters of Li_2MnO_3 were fitted to the component oxides, MnO_2 and Li_2O rather than Li_2MnO_3 itself and therefore the close accord with the measured structural parameters for Li_2MnO_3 reflects the quality of the potential model. In particular, the potential model parameters were able to reproduce the lattice parameters of pyrolusite and ramsdellite polymorphs of MnO_2 to within 3% and 4%, respectively, of experimental values. In addition, the model predicts (correctly) that the pyrolusite polymorph is energetically more stable compared to ramsdellite.

An exacting test of how accurately the force-field maps the potential hypersurface is to simulate the crystallization of a nanoparticle starting from an amorphous precursor. The potential model used in this present study was used to simulate the crystallization of amorphous MnO_2 into crystalline MnO_2; the MnO_2 crystallised into the pyrolusite polymorph in accord with experiment.[10] Similarly, the model was used to simulate the amorphous to crystalline transition of nano-Li_2O where the Li_2O conformed to the inverse fluorite structure.[12]

Table 1 Potential parameters of the form: $A \exp\left(\frac{-r_{ij}}{\rho}\right) - C r_{ij}^{-6}$, describing the short-range potential terms between the component ion species of Li_2MnO_3; terms not listed are set to zero. Structural parameters, derived using these models, are also tabulated together with measured values

Interaction	A (eV)	ρ (Å)	C (eV Å^6)	Cation charge (e)
Li^+–Li^+	270000.0	0.143	0.00	0.5
Mn^{4+}–Mn^{4+}	23530.5	0.156	16.00	2.2
O^{2-}–O^{2-}	11782.8	0.234	30.22	−1.1
Li^+–O^{2-}	30000.0	0.154	0.00	
Mn^{4+}–O^{2-}	15538.2	0.195	22.00	

$C2/m$	a (Å)	b (Å)	c (Å)	β (degrees)	Reference
Model	4.975	8.589	4.891	109.94	This work
Bulk	4.937	8.532	5.030	109.46	ref. 13
Nanorod	4.925	8.537	5.035	109.53	ref. 14
Error	+0.7%	+0.7%	−2.6%	+0.4%	

Simulation code

The DLPOLY code was used to perform all the molecular dynamical simulations;[15] the user manual provides comprehensive analytical descriptions and discussion of the molecular dynamics simulations, force fields, boundary conditions, algorithms and parallelization methods used in these simulations.

Generating the atomistic model

The general strategy involves cutting a cube of Li_2MnO_3 from the parent bulk material and amorphising the nanoparticle, under MD simulation, while retaining a crystalline seed at the center. The seed then nucleates crystallization of the whole nanoparticle.

Specifically, a nanocube of Li_2MnO_3, comprising 9000 Li^+ ions, 4500 Mn^{4+} ions and 13 500 O^{2-} ions, was constructed using the GULP code.[16] MD simulation, performed at 1845 and 1850 K for 5 ns under the NVT ensemble (constant number of particles, volume and temperature) was used to amorphise and then recrystallise the nanoparticle. In particular, it was found that performing MD simulation at either 1845 or 1850 K was sufficient to amorphise most of the ions comprising the nanoparticle, yet retain a small crystalline seed at the center, which then nucleated the crystallization. The nanoparticle was then cooled by performing MD simulation at 0 K, which acts effectively as a pseudo minimizer.

The configurational energy of the system, calculated as a function of time is shown in Fig. 1. Initially, the system amorphises and at after about 1 ns the crystalline seed nucleates crystallization of the nanoparticle as evidenced by the drop in the configurational energy. Crystallisation is complete after about 3 ns; the latent heat of crystallization is therefore reflected in the energy different between the first (0–1 ns) and second (2.5–5 ns) plateau in the energy trace, Fig. 1, and is calculated to be about 75 kJ mol^{-1} per unit Li_2MnO_3. We note that the first plateau is not flat; rather it is slightly gradiented.

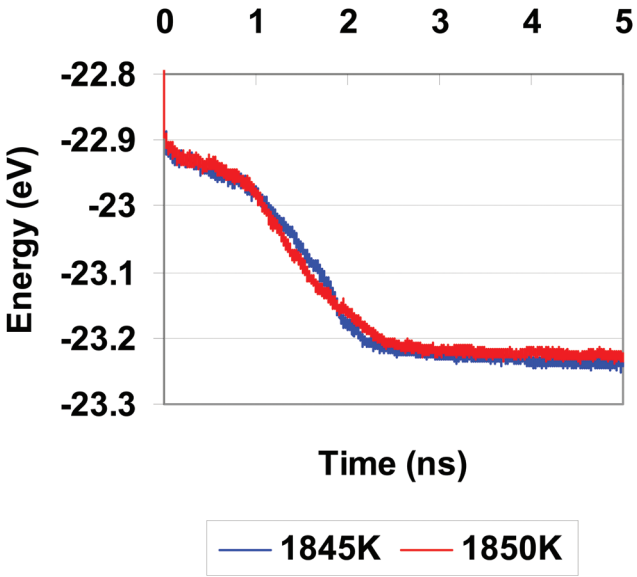

Fig. 1 Configurational energy (10^4 eV) calculated as a function of time for the Li_2MnO_3 nanoparticles simulated at 1845 and 1850 K.

Results

In this section we show the evolution of the structural model, together with microstructural features, such as grain-boundaries and point defects that evolve within the material; the model is validated using experimental data. We then simulate the mobility of Li within the nanomaterial and propose a mechanism for Li transport through the lattice. Finally, we simulate the charging process by sequentially extracting Li from the system and monitoring the structural integrity and Li transport as a function of charge state.

Structural model

The atomistic structures of the starting configuration, amorphous precursor and final, low temperature structure for the nanoparticle simulated at 1845 K, are shown in Fig. 2. We note that the starting configuration, Fig. 2(a), comprises polar sur-

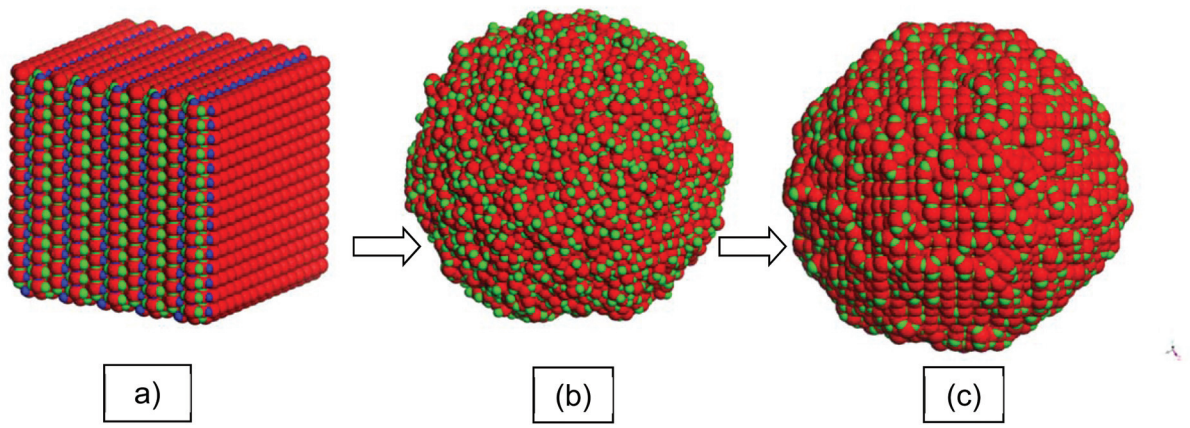

Fig. 2 Atomistic structure of (a) starting configuration, (b) amorphous configuration comprising a crystalline seed at the center, (c) final, low temperature fully crystalline structure. A sphere model representation of the atom positions is used: Mn is colored blue, oxygen is red and Li is green.

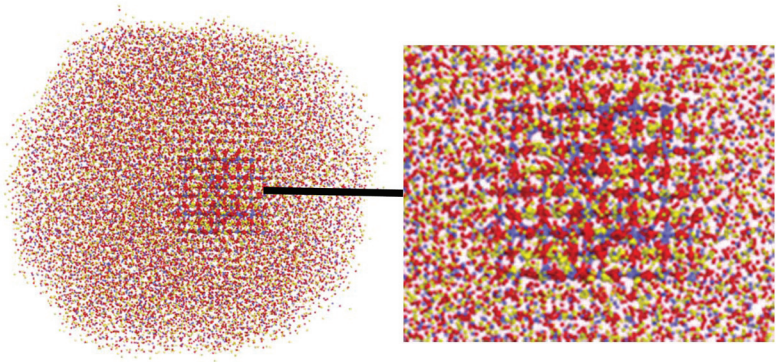

Fig. 3 Atomistic structure of the Li_2MnO_3 nanoparticle after amorphisation revealing the crystalline seed that is retained at its center. A sphere model representation of the atom positions has been used. Mn is colored blue, oxygen is red and Li is yellow.

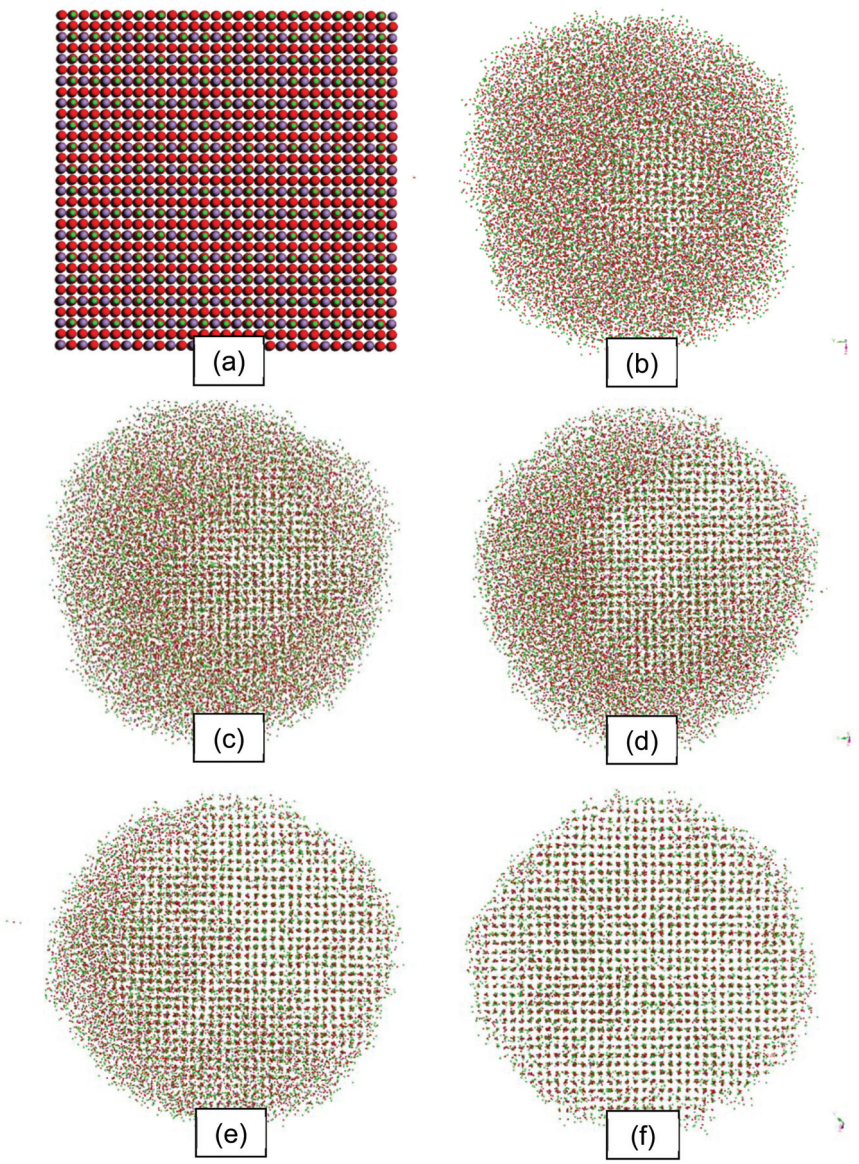

Fig. 4 Atomistic structure of the Li_2MnO_3 nanoparticle during crystallization performed at 1845 K. (a) Starting configuration (0 nanoseconds), (b) after 0.5 ns, (c) 1 ns, (d) 1.3 ns, (e) 1.8 ns, (f) 2.8 ns. The figures can be usefully correlated with the configurational energy, Fig. 1. A sphere model representation of the atom positions is used: Mn is colored blue, oxygen is red and Li is green.

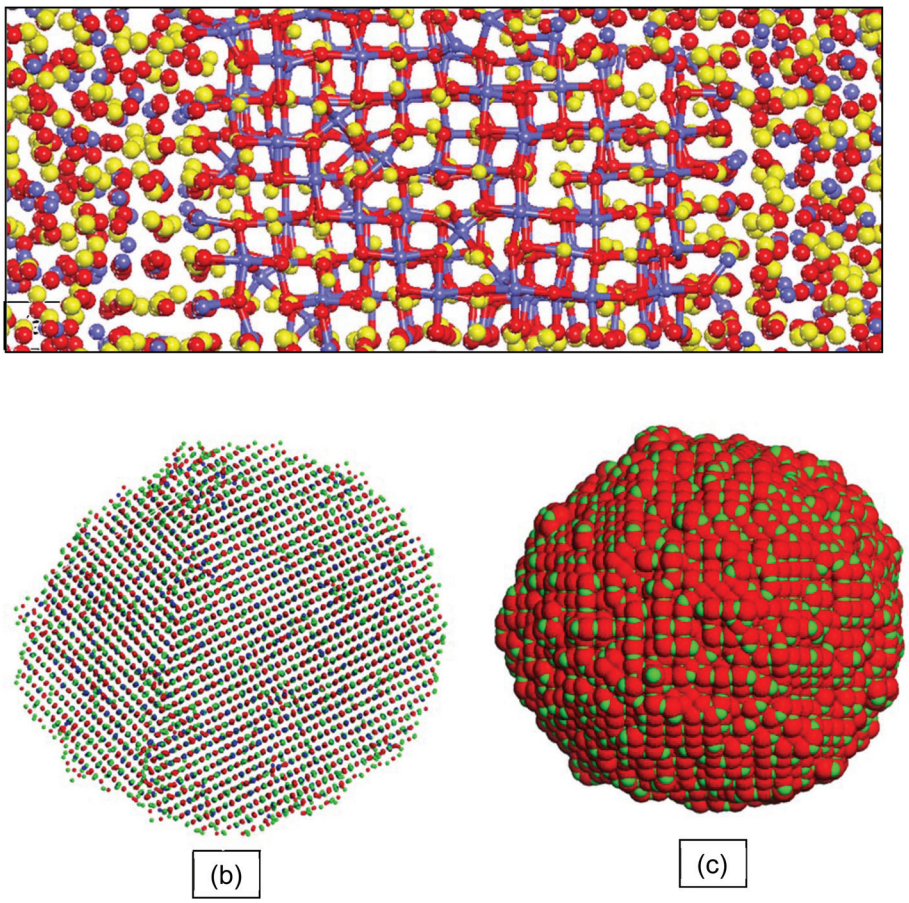

Fig. 5 Atomistic structure of the Li_2MnO_3 nanoparticle crystallised at 1850 K. (a) Atomistic structure of the nucleating seed within the amorphous sea of ions; only a segment of the nanoparticle is shown for reasons of clarity (Li is coloured yellow). (b) Slice cut through the nanoparticle revealing the grain-boundary structure that has evolved within the nanoparticle (Li is green). (c) Final, low energy structure of the nanoparticle (Li is green).

faces,[17] which are unstable. Under MD simulation, the structural instability induces rearrangement of the ions as the system attempts to quench the polar surfaces. This process helps facilitate the crystalline to amorphous transition. We note that during the amorphisation step, the nanoparticle retains a crystalline seed at the center, Fig. 3, which nucleates recrystallization of the amorphous sea of ions during prolonged MD simulation, Fig. 4. In particular, amorphous ions at the crystallization front adhere to the surface of the crystalline seed with crystallization emanating radially from the seed. The final model structure of the Li_2MnO_3 nanoparticle is a single crystal with a distorted rocksalt structure.

In contrast to the single crystal (model) nanoparticle, simulated at 1845 K, the nanoparticle simulated at 1850 K yields a bi-crystal, Fig. 5, and comprises two misoriented crystalline regions separated by a grain-boundary. Previously, we found that grain-boundaries evolve during crystallization because *two* crystalline nucleating seeds spontaneously evolve within the structure before crystallization is complete.[18] In particular, the two crystalline seeds are necessarily misoriented with respect to each other because all orientations are energetically equivalent within an amorphous local environment and as they nucleate crystallization, the two crystallization fronts impinge upon one another facilitating the evolution of the grain boundary. Conversely, in this present study, it is surprising that a bi-crystal evolved because a second crystalline seed did not evolve; rather crystallization emanated from a single seed.

Inspection of the atomistic structure of the nanoparticle during crystallization, Fig. 6, confirms that an additional nucleating seed did not evolve; rather crystallization emanating from the single seed resulted in the evolution of the grain-boundary. In particular, as amorphous ions at the amorphous/crystalline interface condensed onto the surface of the crystalline region, they did not locate on lattice sites, which would have resulted in extending the single crystal; rather they located at misaligned positions, facilitating the evolution of the grain-boundary. An enlarged segment of the system showing the embryonic stages of this misalignment is shown in Fig. 7.

The final low temperature structure for the Li_2MnO_3 nanoparticle, crystallized at 1850 K, is similar to the model nanoparticle crystallised at 1845 K, and conforms to a distorted rocksalt-type structure with interconnecting Oxygen and Mn/Li sublattices, Fig. 8. We also note a high concentration of (Li, Mn and O) vacancies. In addition, we observe no long-range ordering of the Mn or Li positions. In particular, all layers

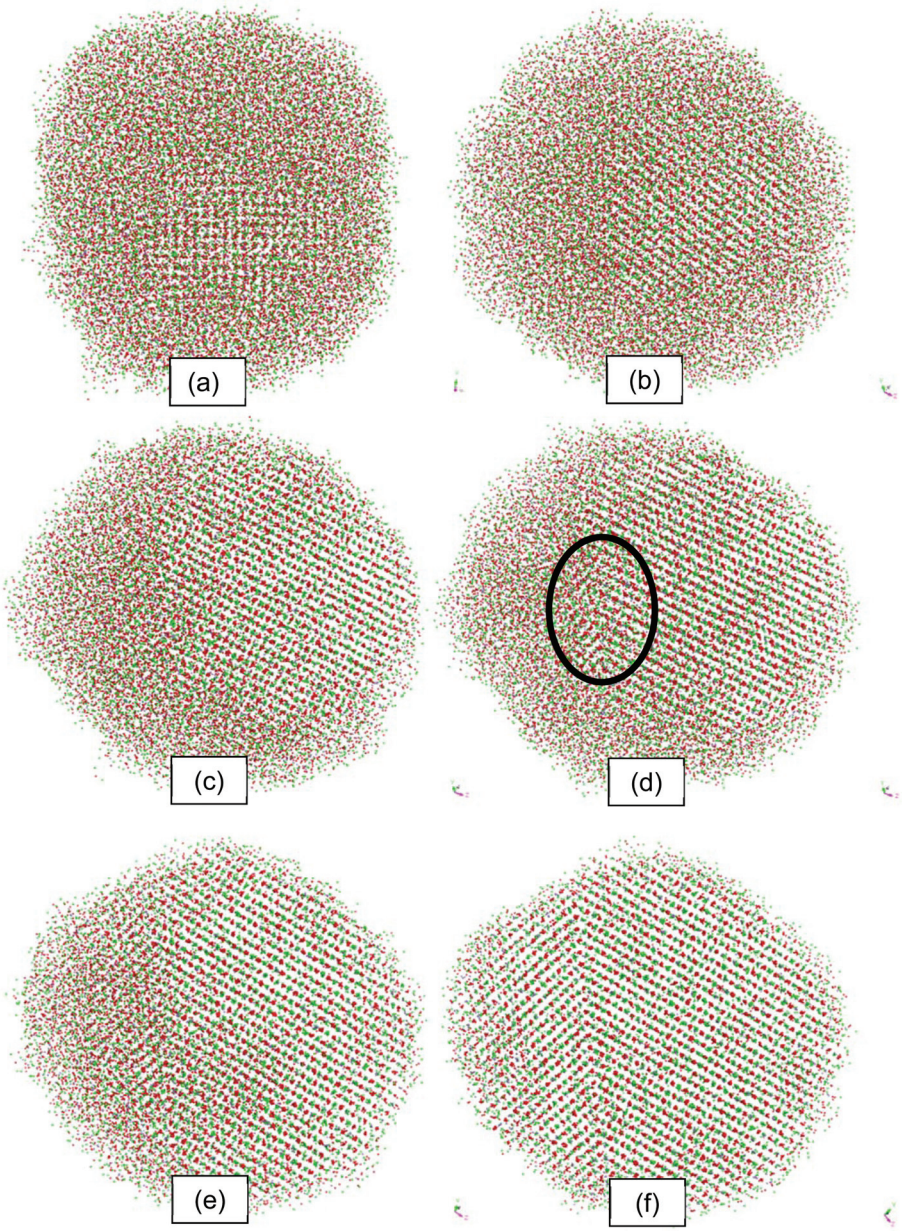

Fig. 6 Atomistic structures of the Li_2MnO_3 nanoparticle as a function of time during crystallisation performed at 1850 K. (a) 0.3 ns, (b) 0.9 ns, (c) 1.35 ns, (d) 1.41 ns, (e) 1.8 ns and (f) 2.4 ns. A sphere model representation of the atom positions is used: Mn is colored blue, oxygen is red and Li is green.

within the model Li_2MnO_3 comprise *mixed* Li and Mn species. The XRD pattern, calculated using the model nano-Li_2MnO_3 structure, is shown in Fig. 8(c) and superimposed with the measured XRD pattern for bulk Li_2MnO_3.[7] The right shift of the simulated XRD trace at lower angles can be attributed to the mixing of the Li and Mn layers. The broad peak at low angles may be attributed to the disorder in the nanocrystalline material. The simulated XRD patterns were calculated using the Materials Studio® suite of programmes.

To better understand the model structure, four cationic layers, cut sequentially from the Li_2MnO_3 model nanoparticle are shown in Fig. 9. The figure reveals that there is mixing of Li and Mn in every layer in contrast to the alternating Li and ($Mn_{2/3}$, $Li_{1/3}$) layers of the parent bulk material. In particular, Mn ions occupy Li sites within the alternating Li layers and can therefore be regarded as point defects. We note that the mixed Li–Mn layers of our model structure are analogous to the mixed cationic layers fabricated by Cho and co-workers,[19]

Energetics

Li_2O can be extracted from Li_2MnO_3 *via* acid leaching.[4] The drive to perform this reaction was to fabricate MnO_2, which can be used as an insertion electrode.

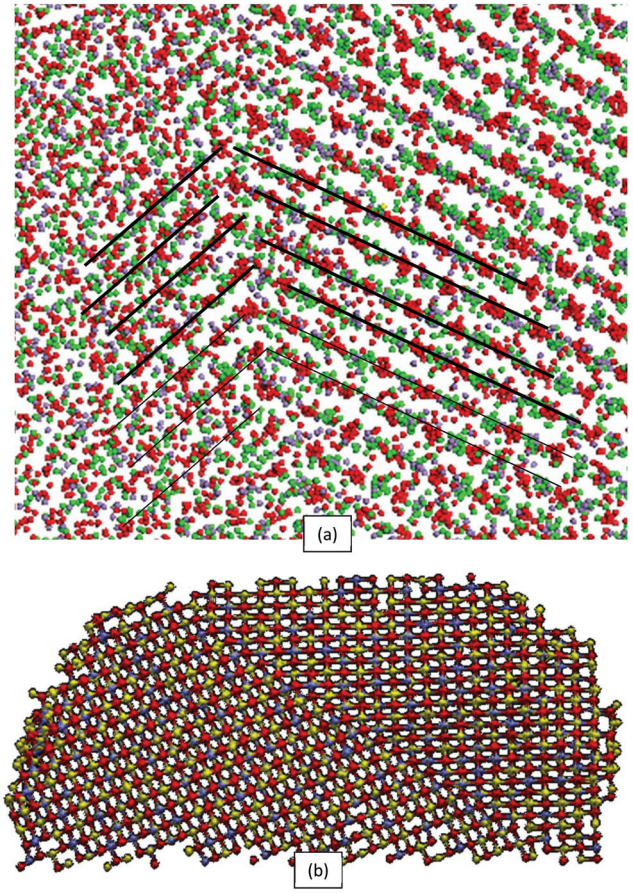

Fig. 7 (a) Atomistic structure of a segment of the Li_2MnO_3 nanoparticle showing the embryonic stages of the evolution of the grain-boundary. Thick and thin lines reveal more clearly the atomic planes. (b) Segment of the nanoparticle at the end of the crystallization showing more clearly the grain-boundary structural configuration. A sphere model representation of the atom positions is used: Mn is colored blue, oxygen is red and Li is either green (top) or yellow (bottom).

$$Li_2MnO_3 \rightarrow Li_2O + MnO_2$$

To calculate the energetics of this reaction a nanoparticle of MnO_2 conforming to the pyrolusite structure and Li_2O, conforming to the inverse fluorite structures were generated using simulated amorphisation and recrystallization.[10,12] The total energy for the reaction was then calculated as the energy of the component Li_2O and MnO_2 nanoparticles minus the energy of the Li_2MnO_3 nanoparticle. The calculated energy for the reaction is +67 kJ mol^{-1} suggesting that the Li_2MnO_3 nanoparticle is more stable with respect to the component Li_2O and MnO_2 nanoparticles (Table 2).

We also note that the energy difference between the Li_2MnO_3 nanoparticles with and without a grain-boundary is 0.15 kJ mol^{-1}. However, this is not wholly the energy associated with the grain-boundary; rather it includes additional structural differences such as the precise atomic configuration including surface and sub-surface ionic relaxation.

Li mobility

To operate as a battery, Li must enter and be extracted from the host material; its mobility within the host is therefore central to this process. To this end we used the atomistic models of Li_2MnO_3 to simulate Li mobility within the lattice to identify mechanisms for Li transport in the lattice. In particular, we heated the model nanoparticle comprising a grain-boundary to 1850 K for 300 ps and used molecular graphics to track the motion of Li ions within the lattice, Fig. 11. The mechanism for Li mobility was then determined by analysing the trajectory files using molecular graphics. The mobility was found to be vacancy driven with Li moving from their lattice positions to neighboring vacancies, Fig. 12. We also noticed that on some occasions, Li displaces neighboring Mn ions, Fig. 13.

Fig. 11 shows the mobility of the Li at the start, Fig. 11(a), of the simulation and after 300 ps, Fig. 11(b). In particular, all the ions within a slice, Fig. 11(a), were represented by large spheres. After 300 ps, one can observe, Fig. 11(b), that some of the Li ions have moved half the diameter of the nanoparticle. Analysis using graphical techniques revealed that the fastest moving Li ions are located on the surface of the nanoparticle, but also some Li ions traversed the body of the nanoparticle to reach the surface.

Experimentally, the perfect bulk Li_2MnO_3 crystal structure conforms to a $C2/m$ structure,[20] Fig. 8(c), and is best described as $Li[Mn_{2/3}, Li_{1/3}]O_2$ because it comprises alternating Li and $Mn_{2/3}$, $Li_{1/3}$ cationic sublattices; there has been some controversy over the precise detail of the structure; for example see ref. 21 The material is known to be electrochemically inactive for Li intercalation or deintercalation.[4] Conversely, a study on the electrochemistry of nanocrystalline Li_2MnO_3, with a crystallite size of 5 nm, showed 'the ability of the nanocrystalline compound to allow large capacity, reversible Li intercalation with excellent cycling performance, in sharp contrast to the microcrystalline Li_2MnO_3'.[7] The study identified that Mn exists in the 4+ oxidation state and in a local atomic/electronic environment similar to that in the rocksalt monoclinic Li_2MnO_3; the nanocrystallites were defective and disordered and lacked long-range ordering of Mn and Li species.

In Fig. 14 we propose an idealised mechanism to help rationalise why the nanoform of Li_2MnO_3 is electrochemically active whereas, conversely, the bulk parent material is inactive. In particular, our models of nano-Li_2MnO_3 comprise Mn (defect) ions in the Li planes, Fig. 14(a) in contrast to the alternating Li and ($Mn_{2/3}$, $Li_{1/3}$) planes in the parent bulk material, Fig. 14(d). During deintercalation of Li in nano-Li_2MnO_3, the Mn 'defect scaffold' holds open the channels maintaining the integrity host lattice structure enabling intercalation of Li back into the host lattice, Fig. 14(b, c) and facilitating charge–discharge cycling. Conversely, for the parent bulk material, there are no Mn ions to maintain the structural integrity of the channels, Fig. 14(e, f), during deintercalation.

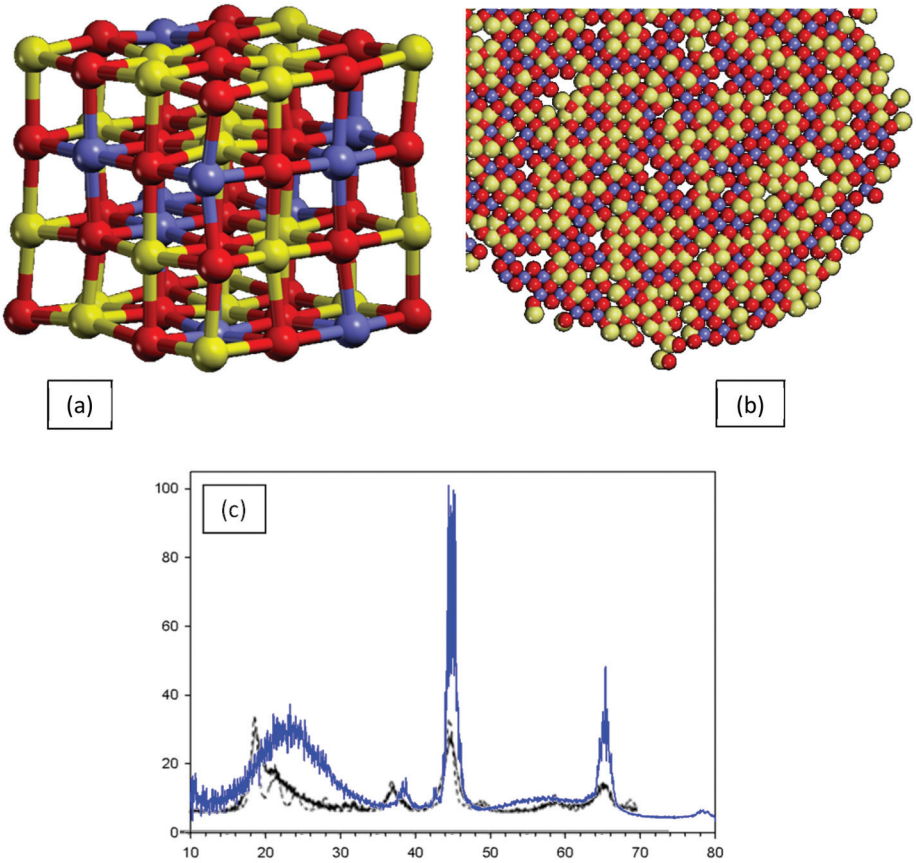

Fig. 8 Atomistic structure of a model Li_2MnO_3 nanoparticle. (a) Ball and stick representation of the atom positions showing a segment of the distorted rocksalt-type structure. (b) Slice cut through the nanoparticle showing the Li, Mn and oxygen atoms together with cationic and anionic vacancies. (c) Calculated XRD (blue trace – this work) compared to the measured (solid black trace) XRD for bulk Li_2MnO_3, and (dashed black trace) simulated bulk Li_2MnO_3 reproduced with permission from ref. 7 American Chemical Society copyright 2005. Li ions are colored yellow; Mn is blue and oxygen red.

Our models, for the nanocrystalline form of Li_2MnO_3, Fig. 14, accord with the presence of pillar ions fabricated by Cho and co-workers;[19] our models are also highly disordered with no long-range ordering of Mn, Li cations in accord with the findings of Jain and co-workers.[7] The structural accord therefore adds credibility to our prediction that Li mobility within the nanomaterial is vacancy driven.

We note that the presence of Mn ions in all Li layers enables a continuous network of channels in three dimensions enabling Li to move in all spatial directions to facilitate intercalation and deintercalation.

The charging process

To determine the structural integrity of the nanomaterial and Li mobility during charging, Li_2O was extracted from the model Li_2MnO_3 nanoparticle to facilitate $Li_{2-2x}MnO_{3-x}$. Specifically, 0, 500, 1000 and 1500 Li ions, together with charge compensating oxygen ions, were extracted from the model nanomaterial at random positions. The mobility of the residual Li through the lattice after each sequential extraction was then calculated by performing MD simulation at 1500 K.

The ionic self-diffusion can be determined from calculated mean square displacements (MSD) over N ions following:

$$\mathrm{MSD} = \langle r_i^2(t)\rangle = \frac{1}{N}\sum_{1}^{N}[r_i(t) - r_i(0)]^2,$$

where r_i is the distance, r, moved by ion, i, at time t. The diffusion coefficient, D_i, can then be extracted from the MSD following:

$$\langle r_i^2(t)\rangle = 6D_i(t) + B,$$

where B is the Debye–Waller factor. The mobility of the Li ions, calculated as a function of depth of charge (Li_2O extracted) is shown in Fig. 15. The simulations reveal that the Li ion mobility increases with depth of charge; calculated diffusion coefficients are: 1.6, 1.9, 2.1 and 2.6 ($\times 10^{-5}$ cm^2 s^{-1}) for charge depths corresponding to 0% (0 Li), 5.5% (500 Li), 11% (1000 Li) and 17% (1500 Li) of the theoretical maximum.

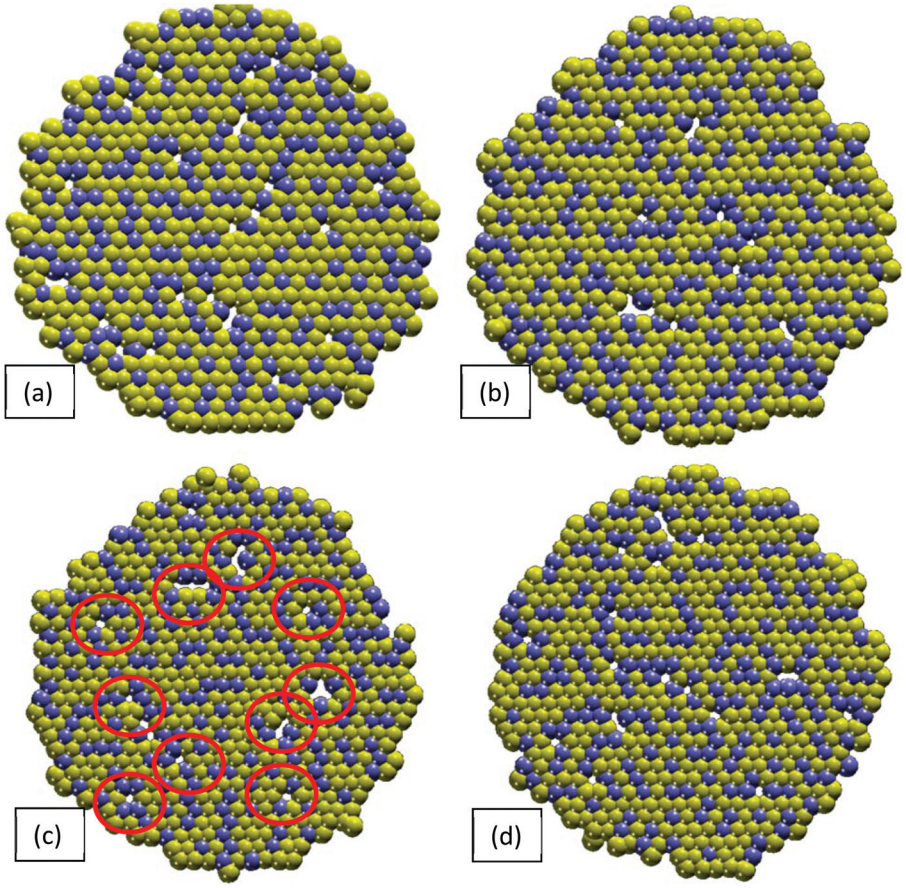

Fig. 9 Atomistic structures of four, (a)–(d), sequential cationic layers in the model Li_2MnO_3 nanoparticle revealing that there are no layers comprising wholly Li ions. The images also show vacancies that have evolved within the layers highlighted with red ovals in (c).

Table 2 Energies calculated for the MnO_2, Li_2O and Li_2MnO_3 nanoparticles

	MnO_2 nano particle	Li_2O nano particle	Li_2MnO_3 nano particle
Total Li^+ ions	—	17 576	9000
Total Mn^{4+} ions	8232	—	4500
Total O^{2-} ions	16 464	8788	13 500
Total ions	24 696	26 364	27 000
Number of neutral units	8232	8788	4500
E (0 K)/eV for the system	−336486.6 eV	−102691.3 eV	−239657.2 eV
E (0 K) per neutral unit	−40.88 eV	−11.685 eV	−53.257 eV
$Li_2O + MnO_2 \rightarrow Li_2MnO_3$	−0.7 eV (−67 kJ mol^{-1})		

The defect structures of the uncharged and 17% charged material are shown in Fig. 16. A slice cut through the alternating oxygen and Li–Mn layers for the uncharged (parent) material is shown in Fig. 16(a–c). The Li–Mn layer is shown in Fig. 16(a, b) and reveals the close packing of Li and Mn ions within the layer. A Li–Mn layer in the 17% charged material, Fig. 16(d, e) reveals the Li and Mn ions are heavily disordered compared to the close packing observed in the uncharged parent material. Slices showing the oxygen layer in the uncharged, Fig. 16(c), and 17% charged material, Fig. 16(f), reveal a much higher concentration of oxygen vacancies in the 17% charged material compared to the uncharged material as expected although the packing is predominantly close-packed for both systems in contrast to the Li–Mn layers.

Inspection of the surface of the 17% charged nanoparticle using graphical techniques, reveals that (similar to) pyrolusite-structured 1 × 1 tunnels terminate at the surface, Fig. 16(g), together with (similar to) ramsdellite-structured (2 × 1) tunnels, Fig. 16(h), albeit there is a much lower concentration of the latter on the surface. Such tunnels facilitate the deintercalation and intercalation of Li during charge–discharge cycling; Li ions were observed to exit the lattice through the tunnels during the MD simulations.

The structure of a layer cut through a model nanoparticle of MnO_2 is shown in Fig. 16(j), revealing the 1 × 1 pyrolocite tunnels within the nanoparticle in which the Li ions intercalate and reside. The structure can be usefully compared to the Li, Mn layers shown in Fig. 16(a, d), which reveal that the material comprises pseudo-pyrolusite/ramsdellite channels.

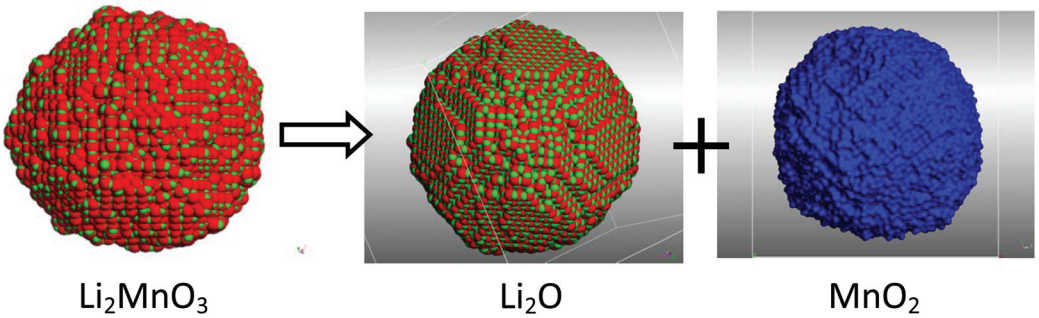

Fig. 10 Atomistic structures of model Li_2MnO_3, Li_2O and MnO_2 nanoparticles used to calculate the energetics of the $Li_2MnO_3 \rightarrow Li_2O + MnO_2$ reaction.

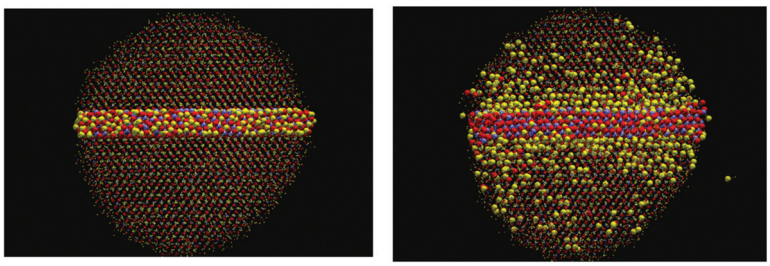

Fig. 11 Molecular graphical representations of the model Li_2MnO_3 nanoparticle used to observe the mobility of Li through the lattice. Left: Starting structure. Right: After performing MD simulation for 300 ps at 1850 K revealing that the Li ions can traverse half the diameter of the nanoparticle (5 nm) within this time. Atom positions are represented by small and large spheres, Li is yellow, Mn is blue and oxygen red.

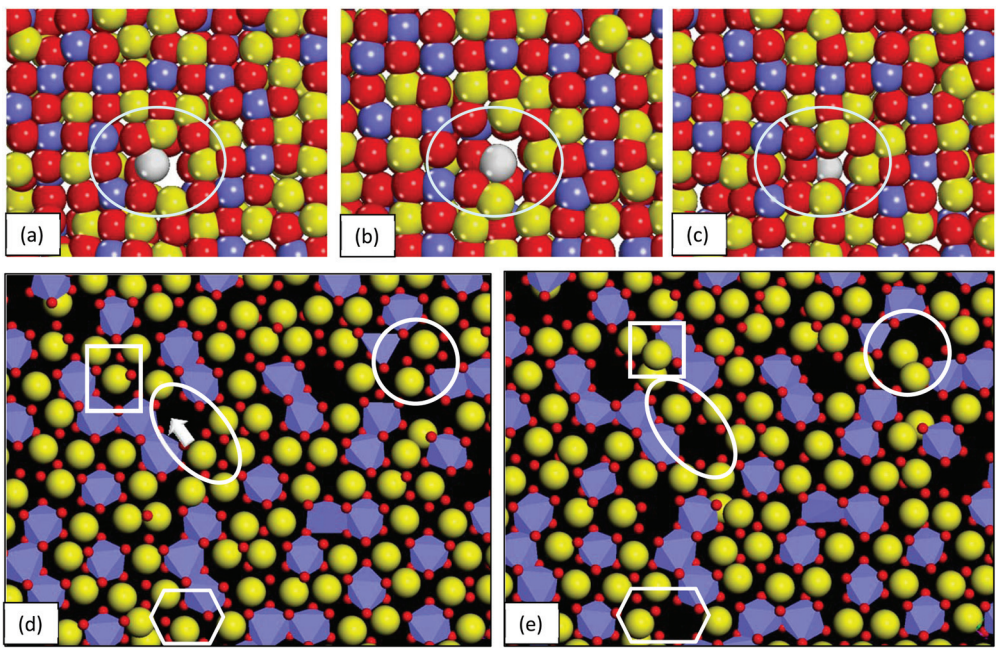

Fig. 12 Snapshots of segments of the Li_2MnO_3 nanoparticle taken as a function of time showing the mechanism underpinning Li transport. (a–c) Sphere model representation of the atom positions, showing a Li ion, coloured white, moving to a vacant position in the lattice. (d, e) Polyhedral rendering of the MnO_6 octahedra and sphere model representation of the Li positions to reveal more clearly the channels in which the Li ions are able to diffuse. A comparison between (d) and (e) reveals the mobility of Li ions within the channels. For example, the Li in the oval (d–e) show Li hopping between adjacent lattice sites within the plane of a Li, Mn layer. The Li in the square, circle and hexagon show Li ions hopping between adjacent Li, Mn layers showing that the Li is able to move in all spatial dimensions within the nanoparticle. Li is coloured yellow, Mn is blue and O is white.

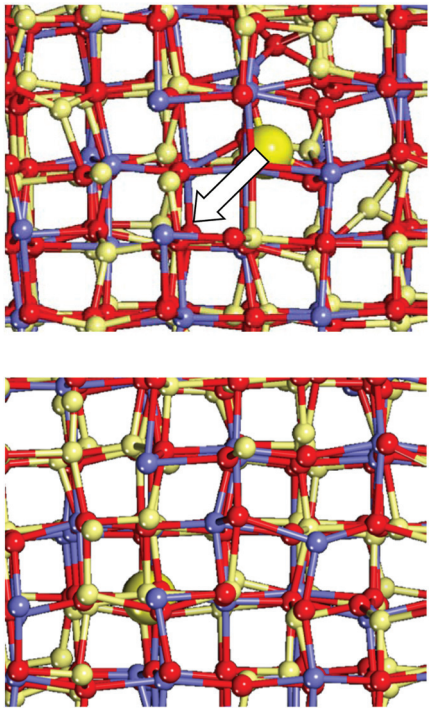

Fig. 13 Ball and stick representation of a segment of the model Li_2MnO_3 nanoparticle showing a Li ion (large yellow sphere) displacing a neighboring Mn ion. Li is colored yellow, oxygen is red and Mn, blue.

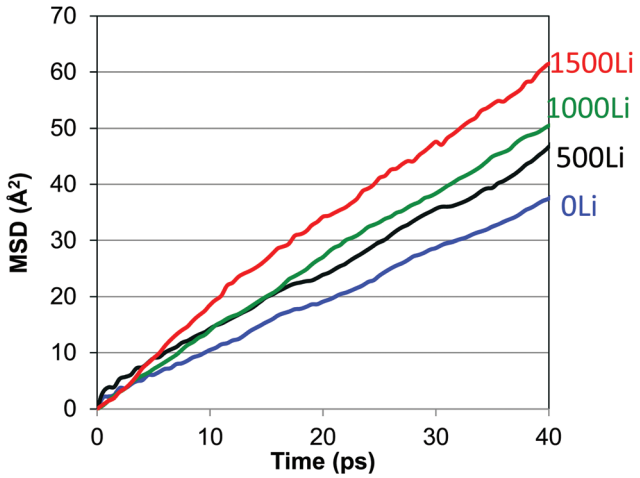

Fig. 15 Mean square displacements of Li ions in Li_2MnO_3, calculated at 1500 K as a function of time, for charge depths corresponding to 0% (0 Li), 5.5% (500 Li), 11% (1000 Li) and 17% (1500 Li) of theoretical maximum.

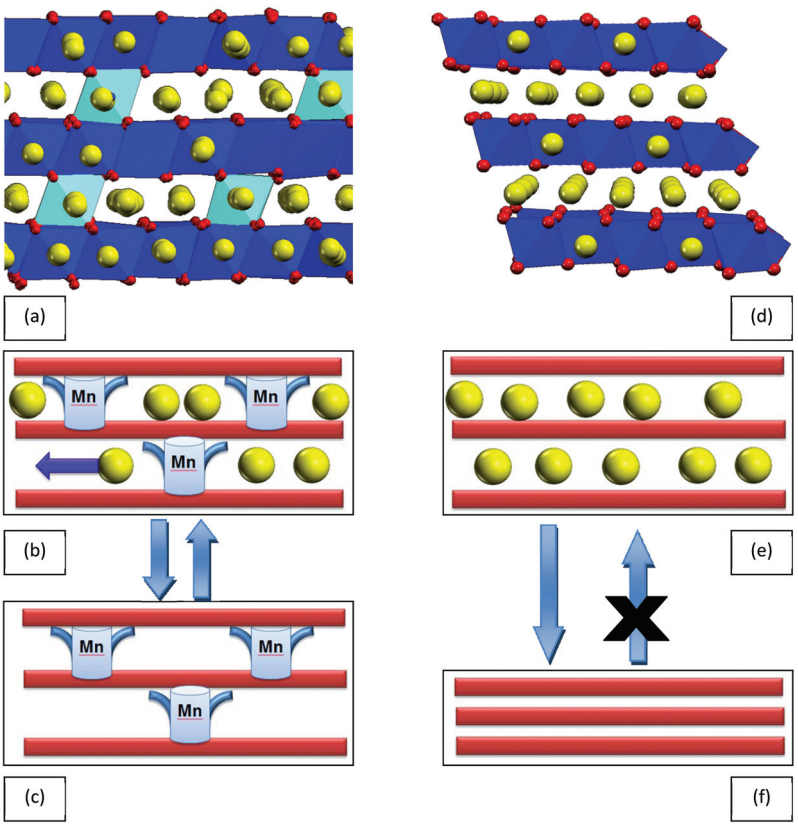

Fig. 14 Atomistic models and schematics to illustrate the proposed electrochemical activity of nano-Li_2MnO_3 compared to the electrochemically inactive parent bulk material. (a) Model structure of nano-Li_2MnO_3 showing Mn ions (coloured light blue) within the Li layers. (b) Schematic of (a) showing how the Mn ions act as a 'defect scaffold' and hold open the channels after deintercalation, (c). (d) Model structure of bulk-Li_2MnO_3 showing the Li layers with no Mn defects within the layer. (e) Schematic of (d) before deintercalation and (f) after deintercalation and collapse of the Li layers.

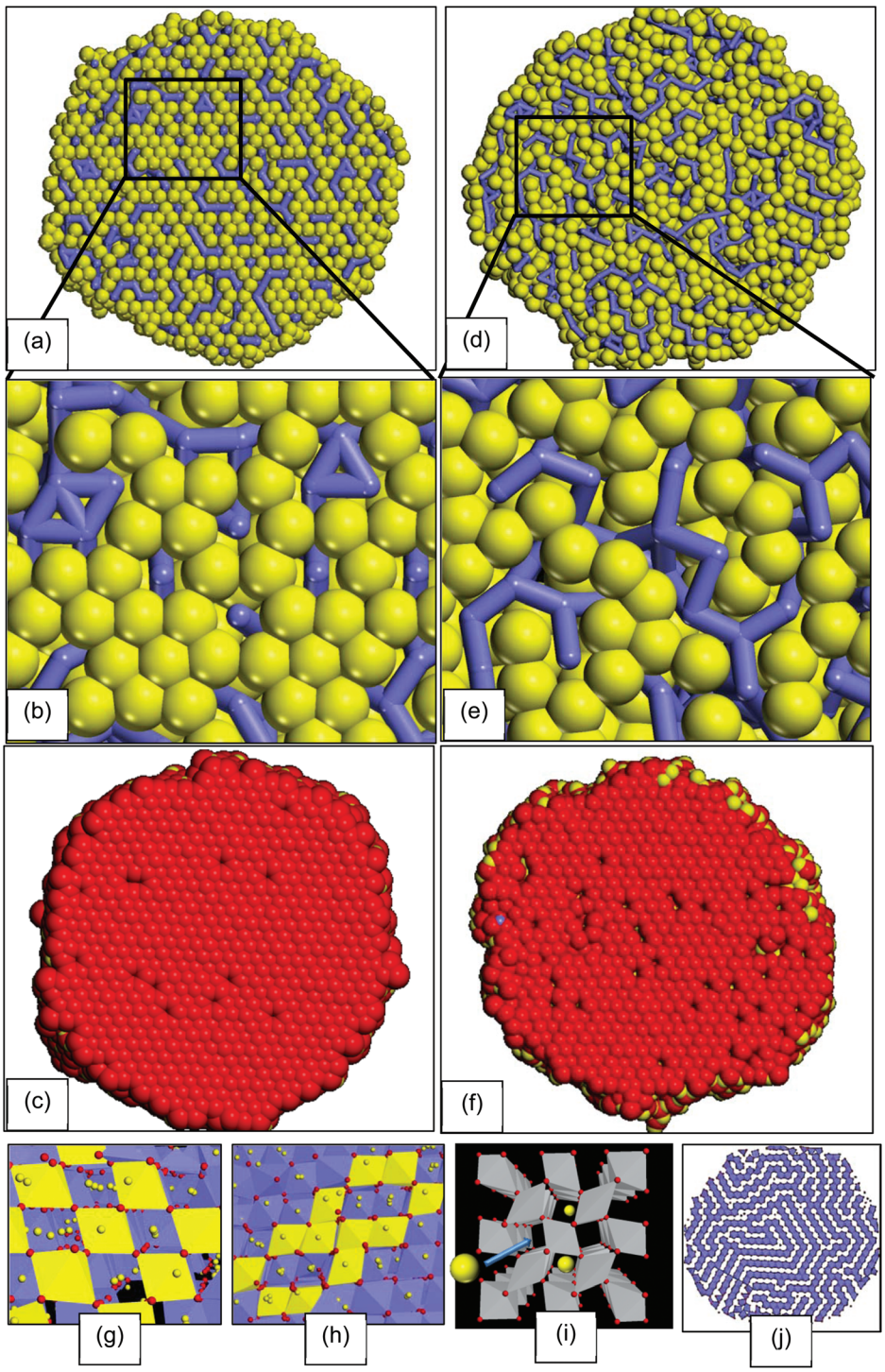

Fig. 16 Atomistic structures of the uncharged (Li_2MnO_3) and 17% charged ($Li_{2-2x}MnO_{3-x}$) material. (a) Plan view of one of the Mn–Li layers in the uncharged material, which is enlarged in (b). (c) Plan view of one of the oxygen layers in the uncharged material. (d) Plan view of one of the Mn–Li layers in the 17% charged material, which is enlarged in (e). (f) Plan view of one of the oxygen layers in the 17% charged material. (g) Region of the surface of the 17% charged material where 1D tunnels with pyrolusite (1 × 1) structure terminate enabling Li ions to intercalate and deintercalate from the host lattice. (h) Region of the surface of the 17% charged material where 1D tunnels with ramsdellite (2 × 1) structure terminate enabling Li ions to intercalate and deintercalate from the host lattice. (i) Schematic of the perfect pyrolusite (isostructural with rutile TiO_2) structure to compare with (g) and (h). Atomistic structure of an Mn, O layer in the MnO_2 nanoparticle, Fig. 10, showing the 1D (pyrolusite) tunnels within the layer in which Li ions can intercalate. Li is coloured yellow, Mn is blue and O is red.

The network of tunnels are interconnected in all spatial dimensions and is facilitated by microtwinning.

Discussion

We propose that the concept of a 'point defect scaffold' might also manifest as a more general phenomenon in materials chemistry. For example, it is well known that doping CeO_2 with aliovalent cations can increase the oxide ion conductivity;[22] the conductivity depends upon both the size of the dopant, its concentration and dispersion. Doping thus imposes a strain-state upon the host material; it has been shown the energy barriers for oxide ion conductivity can be manipulated *via* strain-tuning.[23] Similarly, a maximum in the fluoride-ion conductivity in BaF_2 nanoparticles is achieved when the material is doped with 50% Ca.[24] Here, the difference in size between the Ba (host) and Ca (dopants) induces a strain state into the nanoparticle, which facilitates optimum fluoride-ion conductivity.

In contrast to interfaces, where a misfit can be used to engineer a biaxial strain-state within the overlying thin film,[25] 'point defect scaffolds' can induce strain in either two or three dimensions.

A recent study by Lee and co-workers,[26] showed that oxides, which comprise cation disorder, can be potential candidates for electrodes in rechargeable Li-ion batteries; previously such structures 'were disregarded because of assumptions that Li diffusion tends to be limited by their structures'. Conversely, the study by Lee *et al.* showed that Li diffusion can be facile in the disordered material. Specifically, they used *ab initio* calculations to show that this unexpected behavior is due to percolation of a 'certain type of active diffusion in disordered Li-excess materials'. The work therefore supports our findings in that high Li diffusion is facilitated by maintaining a continuous network of connected channels during deintercalation. Moreover, Lim and co-workers found that nanoparticulate Li_2MnO_3 exhibited high charge capacity 'without any drastic capacity fading' in contrast to the parent bulk material.[27]

Conclusion

Simulated amorphisation and recrystallization has been used to generate atomistic models for nanocrystalline-Li_2MnO_3. To help facilitate crystallization, a crystalline seed was allowed to remain within the center of the nanoparticle, which nucleated the crystallization of the surrounding amorphous sea of ions; without the seed the nanoparticle remained amorphous throughout the MD simulation. Performing the MD simulation at 1845 K resulted in a single crystal nanoparticle. Conversely, a bi-crystal evolved during simulated crystallization at 1850 K. Specifically, a grain-boundary developed as the (amorphous) ions, within the crystallization front, became misaligned as they condensed onto the surface of the crystalline region. Clearly, subtle changes in simulation conditions pertaining to the crystallization can influence profoundly the microstructure. Our calculations also predict that the nano-Li_2MnO_3 is 67 kJ mol^{-1} more stable compared to the component Li_2O and MnO_2 nanocrystals.

The final crystal structures for the nanoparticles are highly defective with Li, Mn and O vacancies and comprise mixing of Li and Mn in all layers in contrast to the parent bulk material, which has alternating Li and ($Mn_{2/3}$, $Li_{1/3}$) layers. The final structural models were interrogated to determine the mechanisms of Li mobility, which was found to be vacancy driven.

We propose that the reason nanocrystalline-Li_2MnO_3 is electrochemically active, in contrast to the parent bulk-Li_2MnO_3, is because in the nanomaterial, the alternating Li planes are held open by Mn atoms, which act as a 'point defect scaffold'. In particular, during deintercalation, the Li ions move out of the Li layer but this does not lead to structural collapse of the nanostructure because Mn ions (as point defects) exist within this layer and hold it open, thus maintaining the structural integrity of the material – specifically, the three-dimensional network of channels, through which the Li ions are able to diffuse, are maintained during charge–discharge cycling. Accordingly, oxides that comprise cation disorder, can be potential candidates for electrodes in rechargeable Li-ion batteries.

Such observation epitomizes the need to develop models that capture the hierarchical structural complexity of the real material. Specifically, by simulating directly the crystallization process, Mn ions were able to crystallize within both the Li, Mn and Li layers.

Acknowledgements

South African Research Chair Initiative of the Department of Science and Technology, and the National Research Foundation.

References

1 P. G. Bruce, B. Scrosati and J. M. Tarascon, Nanomaterials for Rechargeable Lithium Batteries, *Angew. Chem., Int. Ed.*, 2008, **47**, 2930–2946.

2 D. A. Tompsett and M. S. Islam, Electrochemistry of Hollandite alpha-MnO2: Li-Ion and Na-Ion Insertion and Li2O Incorporation, *Chem. Mater.*, 2013, **25**, 2515.

3 T. X. T. Sayle, R. R. Maphanga, P. E. Ngoepe and D. C. Sayle, Predicting the Electrochemical Properties of MnO2 Nanomaterials Used in Rechargeable Li Batteries: Simulating Nanostructure at the Atomistic Level, *J. Am. Chem. Soc.*, 2009, **131**, 6161.

4 M. M. Thackeray, C. S. Johnson, J. T. Vaughey, N. Li and S. A. Hackney, Advances in manganese-oxide 'composite' electrodes for lithium-ion batteries, *J. Mater. Chem.*, 2005, **15**, 2257.

5 J. R. Croy, K. G. Gallagher, M. Balasubramanian, B. R. Long and M. M. Thackeray, Quantifying Hysteresis and Voltage Fade in xLi2MnO3•(1-x)LiMn0.5Ni0.5O2 Electrodes as a Function of Li2MnO3 Content, *J. Electrochem. Soc.*, 2014, **161**(3), A318–A325.

6 M. M. Thackeray, *Prog. Solid State Chem.*, 1997, **25**, 1.

7 G. R. Jain, J. S. Yang, M. Balasubramanian and J. J. Xu, Synthesis, electrochemistry, and structural studies of lithium intercalation of a nanocrystalline Li2MnO3-like compound, *Chem. Mater.*, 2005, **17**, 3850.

8 F. W. Zhang, A. M. Walker, K. Wright and J. D. Gale, Defects and dislocations in MgO: atomic scale models of impurity segregation and fast pipe diffusion, *J. Mater. Chem.*, 2010, **20**, 10445.

9 A. S. Barnard, Modelling of nanoparticles: approaches to morphology and evolution, *Rep. Prog. Phys.*, 2010, **73**, 086502.

10 T. X. T. Sayle, C. R. A. Catlow, R. R. Maphanga, P. E. Ngoepe and D. C. Sayle, Generating MnO(2) nanoparticles using simulated amorphization and recrystallization, *J. Am. Chem. Soc.*, 2005, **127**, 12828.

11 T. X. T. Sayle, P. E. Ngoepe and D. C. Sayle, Simulating Mechanical Deformation in Nanomaterials with Application for Energy Storage in Nanoporous Architectures, *ACS Nano*, 2009, **3**, 3308.

12 T. X. T. Sayle, P. E. Ngoepe and D. C. Sayle, Generating structural distributions of atomistic models of Li_2O nanoparticles using simulated crystallisation, *J. Mater. Chem.*, 2010, **20**, 10452–10458.

13 P. Strobel and B. Lambert-Andron, *J. Solid State Chem.*, 1988, **75**, 90.

14 X. O. Wang, J. M. Song, L. S. Gao, H. G. Zheng, M. R. Ji and Z. Zhang, Synthesis of single crystalline layered lithium manganese oxide nanorods, *Solid State Commun.*, 2004, **132**, 783.

15 W. Smith, T. R. Forester and I. T. Todorov, http://www.stfc.ac.uk/cse/25526.aspx.

16 J. D. Gale, GULP: Capabilities and Prospects, *Z. Krist.*, 2005, **220**, 552–554.

17 J. Goniakowski, F. Finocchi and C. Noguera, Polarity of oxide surfaces and nanostructures, *Rep. Prog. Phys.*, 2008, **71**, 016501.

18 D. C. Sayle, X. D. Feng, Y. Ding, Z. L. Wang and T. X. T. Sayle, "Simulating synthesis": Ceria nanosphere self-assembly into nanorods and framework architectures, *J. Am. Chem. Soc.*, 2007, **129**, 7924.

19 Y. Cho, P. Oh and J. Cho, A New Type of Protective Surface Layer for High-Capacity Ni-Based Cathode Materials: Nanoscaled Surface Pillaring Layer, *Nano Lett.*, 2013, **13**, 1145–1152.

20 C. H. Lei, J. G. Wen, M. Sardela, J. Bareño, I. Petrov, S.-H. Kang and D. P. Abraham, Structural study of Li2MnO3 by electron microscopy, *J. Mater. Sci.*, 2009, **44**, 5579–5587.

21 A. Boulineau, L. Croguennec, C. Delmas and F. Weill, Reinvestigation of Li2MnO3 Structure: Electron Diffraction and High Resolution TEM, *Chem. Mater.*, 2009, **21**, 4216.

22 L. Malavasi, C. A. J. Fisher and M. S. Islam, Oxide-ion and proton conducting electrolyte materials for clean energy applications: structural and mechanistic features, *Chem. Soc. Rev.*, 2010, **39**, 4370–4387.

23 R. A. DeSouza, A. Ramadan and S. Horner, Modifying the barriers for oxygen-vacancy migration in fluorite-structured CeO2 electrolytes through strain: a computer simulation study, *Energy Environ. Sci.*, 2012, **5**, 5445.

24 A. Duvel, B. Ruprecht, P. Heitjans and M. J. Wilkening, Mixed Alkaline-Earth Effect in the Metastable Anion Conductor Ba1-xCaxF2 ($0 \leq \times \leq 1$): Correlating Long-Range Ion Transport with Local Structures Revealed by Ultrafast 19F MAS NMR, *Phys. Chem. C*, 2011, **115**, 23784–23789.

25 D. Pergolesi, E. Fabbri, S. N. Cook, V. Roddatis, E. Traversa, A. John and J. A. Kilner, Tensile Lattice Distortion Does Not Affect Oxygen Transport in Yttria-Stabilized Zirconia–CeO_2 Heterointerfaces, *ACS Nano*, 2012, **6**(12), 10524–10534.

26 J. Lee, A. Urban, X. Li, D. Su, G. Hautier and G. Ceder, Unlocking the Potential of Cation-Disordered Oxides for Rechargeable Lithium Batteries, *Science*, 2014, **343**, 519–522.

27 J. Lim, J. Moon, J. Gim, S. Kim, K. Kim, J. Song, J. Kang, W. B. Im and J. Kim, Fully activated Li2MnO3 nanoparticles by oxidation reaction, *J. Mater. Chem.*, 2012, **22**, 11772–11777.